JMEPEG (2012) 21:558–563
DOI: 10.1007/s11665-011-9945-9

1059-9495/$19.00

Fracture Toughness of Functionally Graded Steels

Ali Nazari, Jamshid Aghazadeh Mohandesi, and Shadi Riahi

(Submitted April 22, 2010; in revised form January 30, 2011)

In this study, fracture toughness of functionally graded steels in both crack divider and crack arrester configurations has been studied. Spot-welded plain carbon steel and austenitic stainless steel with different thicknesses and arrangements were used as electrodes of electroslag remelting to produce functionally graded steels. Fracture toughness of the specimens in crack divider configuration was found to depend on the arrangements of the primary electrodes' pieces together with the type of the containing phases. In crack arrester configuration, the fracture toughness was found to depend on the crack tip position and the distance of the crack tip with respect to the bainitic or martensitic intermediate layers.

Keywords crack arrester, crack divider, fracture toughness (J_{IC}), functionally graded steels

1. Introduction

Functionally graded materials (FGMs) are multi-phase systems, which their composition varies gradually in some directions to obtain unique mechanical, thermal, and electrical properties that distinguish them from the conventional composites, which in general are of discrete, piecewise nature with sharp interfaces (Ref 1-4). One of the important FGMs is those in which variations in strength appear. Suresh et al. (Ref 5) found first experimental evidence that a gradient in yield stress influences the behavior of cracks. Becker et al. (Ref 6) modeled fracture toughness with cracks perpendicular and along the strength gradient. Bezensek and Hancock (Ref 7) studied the fracture toughness and Charpy impact energy of functionally graded steels (FGSs) produced with laser welding. A method of creating a functionally graded structural member is by transforming its material at cryogenic temperatures has been presented by Skoczen′ (Ref 8). Recently, functionally graded steels with strength gradient were produced from austenitic stainless steel and plain carbon steel using electroslag remelting (ESR) (Ref 9). By selecting appropriate arrangements and thicknesses of the original ferritic steel ($\dot{\alpha}$) and original austenitic steel ($\dot{\gamma}$) as electrodes, it is possible to obtain composites with several layers consist of ferrite, austenite, bainite, and martensite.

$$(\dot{\alpha}\dot{\gamma})_{el} \xrightarrow{R} (\alpha\beta\gamma)_{com}$$
$$(\dot{\gamma}\dot{\alpha}\dot{\gamma})_{el} \xrightarrow{R} (\gamma M\gamma)_{com}$$

where α, β, γ, and M are ferrite, bainite, austenite, and martensite phases in final composite, respectively; el, com, and R are electrode, composite, and remelting, respectively.

Ali Nazari and **Shadi Riahi**, Department of Materials Science and Engineering, Saveh Branch, Islamic Azad University, Saveh, Iran; and **Jamshid Aghazadeh Mohandesi**, Department of Mining and Metallurgical Engineering, Amirkabir University of Technology, Tehran, Iran. Contact e-mail: alinazari84@aut.ac.ir.

As alloying elements such as carbon, chromium, and nickel atoms diffuse, alternating regions with different transformation characteristics are created. The diffusing atoms individually or together stabilize different phases such as bainite or martensite. The thicknesses of bainitic and martensitic layers depend on the thickness of the primary electrodes and process variables (Ref 10).

Transformation characteristics (Ref 9), Charpy impact energy (Ref 10-12), and tensile properties (Ref 13) of FGSs have previously been studied. From the previous works (Ref 10, 11), it was found that the impact energy of FGS specimens in crack divider configuration depends on the thickness and the type of the containing phases. The presented mathematical models in those works (Ref 10, 11) showed that the formation of martensite layer causes some deviations of analytical results from experimental ones. In fact, martensite layer could accelerate the crack growth due to its brittleness and results in the deviation. In addition, in crack arrester configuration (Ref 12), it has been found that the notch tip position is the main factor to affect the impact energy of the composites. In this study, fracture toughness, J_{IC}, of FGSs has been investigated with the starter crack in both crack divider and crack arrester configurations. The difference between this study and the previous studies (Ref 10-12) is the type of the experiment. J_{IC} test is much more accurate than Charpy impact energy test especially in presence of martensite layer. It has been shown that the martensite layer could not affect fracture toughness as a key phase apart of the other phase in crack divider configuration. In addition, in crack arrester configuration, by an accurate model, the fracture toughness could be predicted, while such a model could not be applied for determining Charpy impact energy. Therefore, the aim of this study is to investigate the absorbed energy of the specimens with a more accurate test in both crack divider and crack arrester configurations.

2. Experimental Procedure

Similar to the previous studies (Ref 9-13), a miniature ESR apparatus was used to produce FGSs. The consumed slag was a mixture of 20% CaO, 20% Al_2O_3, and 60%

CaF_2. The original ferritic and austenitic steels, which were employed as electrodes, were commercial-type AISI 1020 (with 0.2wt.% C, 0.3wt.% Si, 0.2wt.% Mn, 0.05wt.% S, and 0.05wt.% P) and AISI 316 (with 0.07wt.% C, 1wt.% Si, 2wt.% Mn, 0.045wt.% S, 0.03wt.% P, 18.15wt.% Cr, and 9.11wt.% Ni) steels.

Different arrangements of ferritic and austenitic steel slices in the form of 2- and 3-piece electrodes were spot welded for remelting. The height of each slice in primary 2-piece $\dot{\alpha}\dot{\gamma}$ electrode was 100 mm. For 3-piece $\dot{\gamma}\dot{\alpha}\dot{\gamma}$ electrode, the height of the middle slice was 25 mm and that of neighboring slices was 87.5 mm.

Remelting was done under a constant power supply of 16 kVA. After remelting, the composite ingots were hot-pressed at 980 °C down to the thickness of 30 mm and then were air-cooled.

Fracture toughness, J_{IC}, test was carried out on 3-point bend specimens at 18 °C. Specimens dimension was in accordance to the ASTM E1820 (Ref 14) and is illustrated in Fig. 1. The notch was machined with 8 mm depth and a 2 mm fatigue pre-crack was created at the end of the notch root by cyclic 3-point loading with a frequency of 10 Hz. The single specimen method using unloading-reloading procedure was performed. After loading the specimen, about 10% of the maximum load was unloaded and then the specimen was reloaded up to the maximum load. Calculation of the maximum load is given in the ASTM E1820 standard (Ref 14).

Fracture toughness of FGS specimens with crack divider (Fig. 2a) and crack arrester (Fig. 2b) configurations was obtained. In crack divider configuration, specimens with the dimensions of $100 \times 30 \times 10$ mm were machined. Afterwards, 5 mm from top and 5 mm from bottom of specimens' height were cut; such as the specimen dimensions changed to $100 \times 20 \times 10$ mm. In crack arrester configuration, from the produced $\alpha\beta\gamma$ composite ingot, eight series of specimens, with the dimension illustrated in Fig. 1, were produced in some manner that the bainite intermediate layers was placed at different positions with respect to the crack tip; in four series of specimens the crack was placed in α and in the other four in γ region. From $\gamma M\gamma$ composite ingot, due to its symmetric configuration, only four series of specimens with different positions of martensite layer were produced.

Fracture toughness of as-received ferritic and austenitic steels, which were annealed at 980 °C and then were air-cooled and fracture toughness of single-phase bainite and martensite with chemical composition and mechanical properties analogous to those of the bainite and martensite layers was also measured. The production method of single-phase specimens with chemical composition and mechanical properties identical to those of the bainitic and martensitic layers have fully discussed in the previous studies (Ref 10, 11). For single-phase martensite, K_{IC} of the specimen was measured according to the

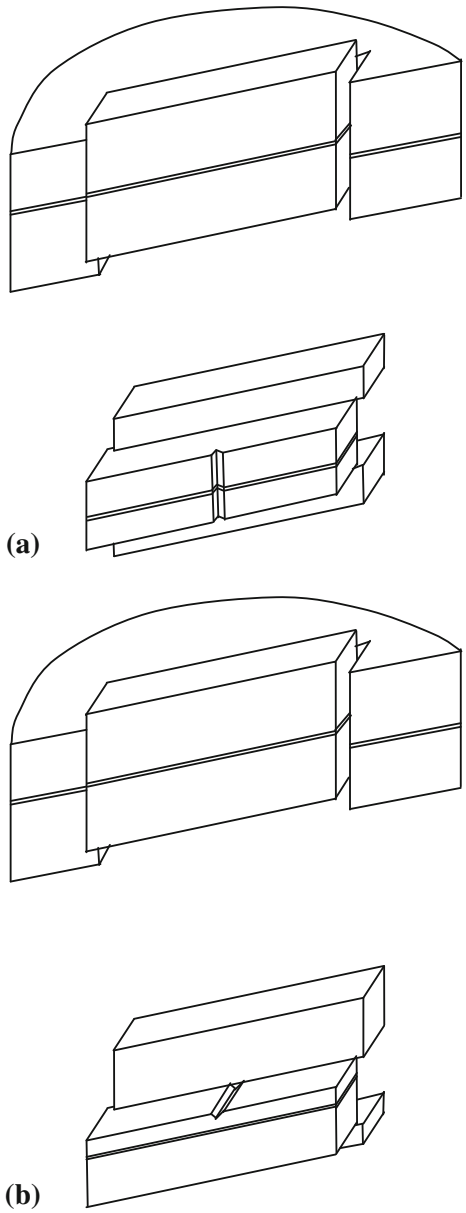

Fig. 2 Microhardness profile of the hot-pressed (a) $\alpha\beta\gamma$ and (b) $\gamma M\gamma$ composite ingots

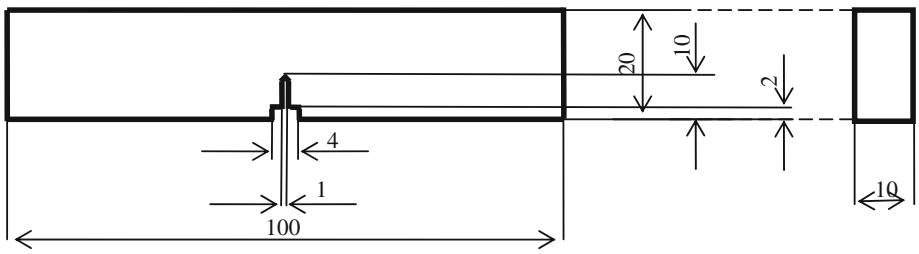

Fig. 1 Dimension of fracture toughness test's specimen (mm)

ASTM E1820 standard (Ref 14) and then J_{IC} of the specimen was calculated according to Eq 1,

$$J_{IC} = \frac{K_{IC}^2(1-\nu^2)}{E} \quad \text{(Eq 1)}$$

where $\nu = 0.3$ is the Poison's ratio and $E = 210$ GPa is the Young modulus.

The dimension of the K_{IC} test specimen was also similar to Fig. 1.

3. Results and Discussion

Figure 3(a) and (b) illustrates Vickers microhardness profile of αβγ and γMγ composites. The thickness of martensite layer is 1.5 mm and that of bainite is 0.6 mm, which was verified by Vickers microhardness examination and is in accordance to the previous studies (Ref 9-13). In addition, Fig. 4 shows the formation of bainite and martensite layers in the produced composites.

Fracture toughness of the composites is shown in Table 1 and that of single-phase specimens is shown in Table 2. Fracture toughness of the specimens is calculated by 0.2 mm offset line from *J-R* curve of the specimens (except for martensite as discussed above).

Table 1 shows that the fracture toughness of αβγ composite in crack divider configuration is more than that of γMγ composite. Although the thickness of austenitic steel (with much more J_{IC} rather than ferritic steel) has been used to produce γMγ composite was larger rather than that of used for αβγ composite, formation of martensite layer causes the reduction in fracture toughness of γMγ composite. Regardless of containing phases, the arrangement of the primary electrode's pieces is a key factor to affect the fracture toughness of the composites. In both αβγ and γMγ composites, an improvement of fracture toughness with respect to the AISI 1020 steel is observed. The improvement of fracture toughness in αβγ composite is superior because of bainite formation with relatively high fracture toughness with respect to the martensite layer and AISI 1020 steel.

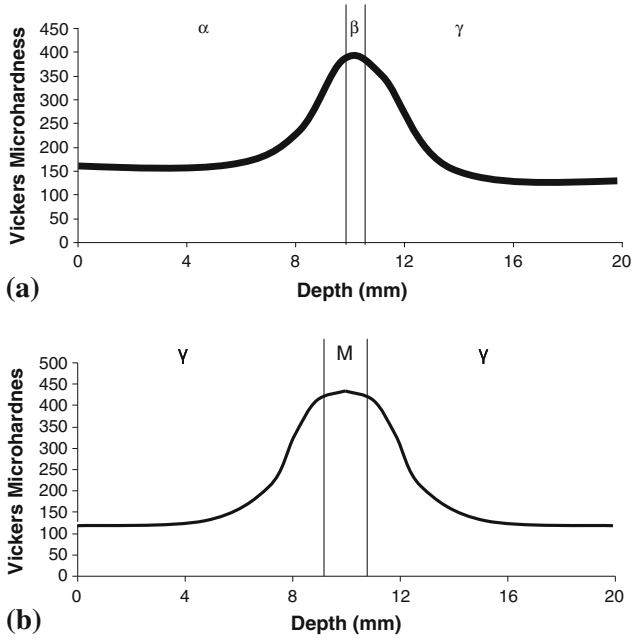

Fig. 3 Microstructure of (a) bainite layer formed in αβγ composite and (b) martensite layer formed between two layers of austenitic region in γMγ composite

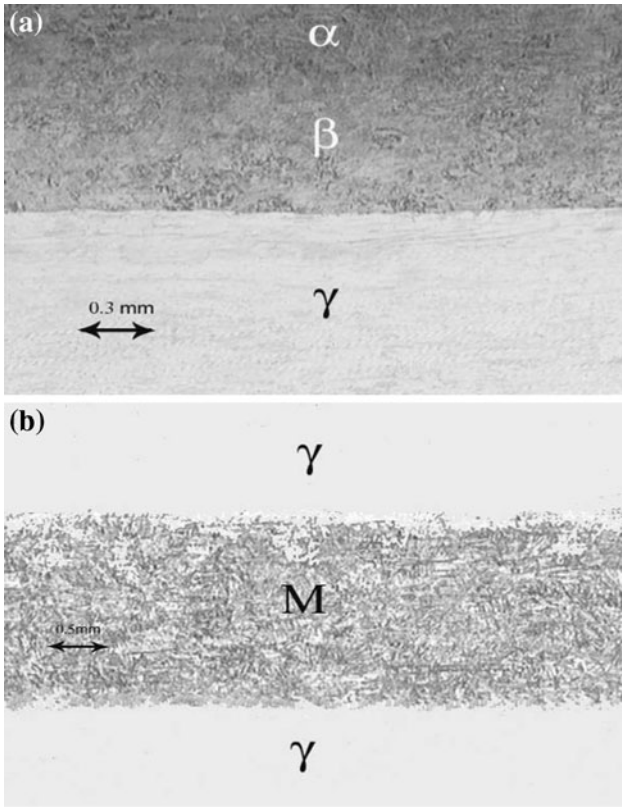

Fig. 4 Preparation of test specimen in (a) crack divider and (b) crack arrester configurations

Table 1 Experimental fracture toughness, J_{IC}, of the composites (kJ/m^2)

		Crack arrester			
	Crack divider	$d = 0$	$d = 1$	$d = 2$	$d = 3$
$\alpha\beta\gamma^{(1)}$	21	31	27	21	14
$\alpha\beta\gamma^{(2)}$		27	33	37	42
γMγ	11	0.16	13	28	34

Crack in (1) is placed at α region and in (2) is placed at γ region for crack arrester configuration
d represent the distance of the crack tip with respect to the bainite or martensite intermediate layers

Table 2 Fracture toughness, J_{IC}, of ferritic steel, austenitic steel, single-phase bainite, and single-phase martensite specimens (kJ/m^2)

Specimen	Ferritic steel	Austenitic steel	Single-phase bainite	Single-phase martensite
Fracture toughness	9	50	29	0.16

Table 1 shows that the fracture toughness of γMγ composite is higher than that of AISI 1020 steel and is lower than that of αβγ composite. Although the thickness of the austenitic phase in γMγ composite is larger than that of αβγ composite, formation of martensite layer causes a considerable reduction in fracture toughness of γMγ composite. However, the presence of austenite phase with high fracture toughness recovers the fracture toughness of γMγ composite. The Charpy impact energy of γMγ composite in crack divider configuration which had been determined by the rule of mixtures (Ref 9, 10) showed a relatively large deviation from the experimental data. It had been argued that the sharp gradient of impact energy adjacent to the newly formed martensite layer inflicts discrepancy in the results (Ref 9, 10). However, in this study, the rule of mixtures is examined for fracture toughness prediction of γMγ composite and as it will be seen, this rule can predict the fracture toughness with more accuracy than Charpy impact energy.

Hutchinson (Ref 15) and Rice and Rosengeren (Ref 16) separately deduced the proportionality between J and the area under stress-strain curve in power-law work-hardened materials. Assuming that αβγ and γMγ composites are composed of graded α and/or γ regions with several layers together with bainite or martensite layers, J_{IC} of each layer in graded regions could be determined from stress-strain curve of that layer. The method of determining the stress-strain curve of the layers have been fully discussed in the previous studies and fracture toughness of composites in crack divider configuration was calculated in accordance to the previous studies (Ref 10, 11) based on the rule of mixtures.

$$J_{IC}^{\alpha\beta\gamma} = \sum_{i=1}^{m_\alpha} J_{IC}(\alpha_i)\cdot V_i + J_{IC}(\beta)\cdot V_\beta + \sum_{i=1}^{n_\gamma} J_{IC}(\gamma_i)\cdot V_i \quad \text{(Eq 2)}$$

$$J_{IC}^{\gamma M\gamma} = 2\cdot\sum_{i=1}^{m_\gamma} J_{IC}(\gamma_i)\cdot V_i + J_{IC}(M)\cdot V_M \quad \text{(Eq 3)}$$

where J_{IC} (α_i) and J_{IC} (γ_i) are the fracture toughness of each layer in α and γ regions, respectively, V_i is the volume fraction of each layer in graded regions (The thickness of each layer was considered 10 μm.), V_β and V_M are the volume fraction of bainite and martensite layers, respectively, J_{IC} (β) and J_{IC} (M) are the fracture toughness of bainite and martensite layers, respectively, m_α and n_γ are the number of layers in α and γ regions of αβγ composite, respectively, and m_γ is the number of layers in γ regions of γMγ composite.

The obtained results from the above equations are listed in Table 3. The agreement between experimental and theoretical results is good despite the reported results for impact energy of FGSs (Ref 10) and laminated composites (Ref 17) which have been deviated from the rule of the mixtures especially in presence of brittle layers.

Table 3 Theoretical fracture toughness, J_{IC}, of the composites (kJ/m^2)

		Crack arrester			
	Crack divider	$d = 0$	$d = 1$	$d = 2$	$d = 3$
αβγ$^{(1)}$	21.8	32.9	28.5	23	15.7
αβγ$^{(2)}$		29.1	35.2	38.4	44.4
γMγ	12.2	0.16	14.7	30.3	35.6

Crack in (1) is placed at α region and in (2) is placed at γ region for crack arrester configuration
d represent the distance of the crack tip with respect to the bainite or martensite intermediate layers

Table 1 shows that the fracture toughness of all produced composites in crack arrester configuration is between that of ferritic steel and austenitic steel. A number of studies have been conducted on fracture energy of layered materials, and it has been reported that fracture energy of them is increased with respect to their constituent materials as a result of the delaminating of the layers when the interface strength between the layers is not high. The stronger the interface, the more difficult the delamination, therefore it diminishes the fracture energies (Ref 17). In this study, since specimens were made by electroslag remelting, interface strength because of atomic diffusion is high justifies the obtained results.

In crack arrester configuration, Table 1 shows that J_{IC} of αβγ composite by situating the crack in α region is always more than J_{IC} of the composite when the crack is situated in γ region (except when the crack is at bainite interface). On the other hand, the closer the crack tip to the bainite layer in α region, the higher the fracture toughness and inversely in γ region, and the closer the crack tip to the bainite layer, the lesser the fracture toughness. This could be discussed in terms of the consumed energy for plastic deformation under J_{IC} test.

Since J_{IC} is the fracture toughness at the beginning of crack propagation, one may consider this energy composed of three portions. A negligible part of energy, which is consumed for elastic deflection of the specimen, a portion consumed for plastic deformation at the location, where force is applied (again this part is able to be neglected because of stress concentration near the crack tip). Finally, the main portion of energy is consumed for plastic deformation ahead of the crack.

By the reason of increasing in the area under stress-strain curve of each layer from α to γ region, one may suppose the increase in J_{IC} value of the layers to follow suit. Thus, a crack in α region encounters an upward J_{IC} gradient; therefore, J_{IC} of the composite becomes more than J_{IC} value of AISI 1020 steel, which J_{IC} of its corresponding layers in comparison with the composite is lower. On the other hand, a crack in γ region experience downward J_{IC} gradient causes lesser J_{IC} of αβγ composite in comparison with AISI 316 steel. In addition, J_{IC} of the composite by situating the crack at α-β and β-γ interfaces is different. Although J_{IC} of the composite is expected to be similar to J_{IC} of the bainite layer in both the conditions, but different plastic deformation zones ahead of the crack (similar to the above discussion) causes different J_{IC} values.

Fracture toughness of γMγ composite in crack arrester configuration with different positions of the crack tip with respect to the martensite layer is also given in Table 1. Reduction of fracture toughness in the presence of martensite layer is very significant; the closer the crack tip to the martensite layer, the lesser the fracture toughness is; similar to αβγ composites, the differences between J_{IC} values of γMγ composites may be explained in terms of plastic deformation energy. Note that due to greater thickness of martensite layer (i.e., 1.5 mm) and much smaller plastic deformation energy ahead of crack with respect to the bainite layer, the difference between fracture toughness of γMγ composite with crack placed at martensite-austenite interface (i.e., $i = 0$) with that of single-phase martensite is not high.

The average J-integral over the specimen thickness in a volume integral form can be obtained as (Ref 17):

$$J = \frac{1}{B}\int_V \left[\sigma_{ij}\frac{\partial u_i}{\partial x_1} - W\delta_{1j}\right]\frac{\partial q_1}{\partial x_j}\mathrm{d}V - \frac{1}{B}\int_V \frac{\partial W}{\partial x_1}q_1\,\mathrm{d}V \qquad \text{(Eq 4)}$$

where B is the specimen thickness, q_1 is a smooth (weight) function in V with a value of unity on the crack front and zero on the surface A, and $\partial W/\partial x_1$ is the explicit derivative of W with respective to x_1 (this term vanishes for homogeneous materials). For a power-law work-hardened material with yield stress σ_y and strain hardening exponent n, the explicit derivative of W with respect to x_1 becomes (Ref 17);

$$\frac{\partial W}{\partial x_1} = \frac{\partial W}{\partial E}\frac{\partial E}{\partial x_1} + \frac{\partial W}{\partial \nu}\frac{\partial \nu}{\partial x_1} + \frac{\partial W}{\partial \sigma_y}\frac{\partial \sigma_y}{\partial x_1} + \frac{\partial W}{\partial n}\frac{\partial n}{\partial x_1} \qquad \text{(Eq 5)}$$

If the properties (σ_y, n, ν, and E) gradient is given, J values can be calculated. Kolednik (Ref 5) has presented a simple solution for a FGM with yield stress gradient in crack arrester configuration while the other parameters are constant. Considering power-law work-hardening in FGSs, based on Kolednik study (Ref 5), the below relation was obtained;

$$\begin{aligned}
J_{\mathrm{tot}} = {} & \frac{F^2a^2(1-\nu^2)}{BEI}\left(1 + 2\frac{F^2f^2\left(\frac{a}{W}\right)}{6\pi\sigma_y^2B^2Wa} + \frac{5}{3}\frac{F^4f^4\left(\frac{a}{W}\right)}{36\pi^2\sigma_y^4B^4W^2a^2} + \frac{1}{2}\frac{F^6f^6\left(\frac{a}{W}\right)}{216\pi^3\sigma_y^6B^6W^3a^3}\right) \\
& - \frac{A'W}{B}\frac{\mathrm{d}}{\mathrm{d}a}\int_0^F \frac{F^n}{r_P(W-a) - \frac{f^2\left(\frac{a}{W}\right)r_P}{6\pi B^2W\sigma_y^2}F^2}\mathrm{d}F - \frac{2}{3}\frac{F^3f'\left(\frac{a}{W}\right)\cdot f\left(\frac{a}{W}\right)(1-\nu^2)}{6\pi m\sigma_y^3EB^3W}\cdot\frac{1-r_P}{r_P} - \frac{(1-\nu^2)W^{\frac{5}{2}}(6\pi)^{\frac{3}{2}}B^2\sigma_y^2}{2mEf^6\left(\frac{a}{W}\right)r_P^2}\cdot \\
& \times\left\{\left[\frac{-1}{2\sqrt{W-a}}\cdot\ln\frac{\sqrt{r_P(W-a)} + \frac{f\left(\frac{a}{W}\right)}{\sigma_yB}\sqrt{\frac{r_P}{6\pi W}}F}{\sqrt{r_P(W-a)} - \frac{f\left(\frac{a}{W}\right)}{\sigma_yB}\sqrt{\frac{r_P}{6\pi W}}F} + \left(\frac{\frac{-r_P}{2\sqrt{r_P(W-a)}} + \frac{f'\left(\frac{a}{W}\right)}{\sigma_yB}\sqrt{\frac{r_P}{6\pi W}}F}{\sqrt{r_P(W-a)} + \frac{f\left(\frac{a}{W}\right)}{\sigma_yB}\sqrt{\frac{r_P}{6\pi W}}F} - \frac{\frac{-r_P}{2\sqrt{r_P(W-a)}} - \frac{f'\left(\frac{a}{W}\right)}{\sigma_yB}\sqrt{\frac{r_P}{6\pi W}}F}{\sqrt{r_P(W-a)} - \frac{f\left(\frac{a}{W}\right)}{\sigma_yB}\sqrt{\frac{r_P}{6\pi W}}F}\right)\sqrt{W-a}\right]\cdot \right. \\
& \left. \times f^3\left(\frac{a}{W}\right) - 3f'\left(\frac{a}{W}\right)\cdot f^2\left(\frac{a}{W}\right)\sqrt{W-a}\cdot\ln\frac{\sqrt{r_P(W-a)} + \frac{f\left(\frac{a}{W}\right)}{\sigma_yB}\sqrt{\frac{r_P}{6\pi W}}F}{\sqrt{r_P(W-a)} - \frac{f\left(\frac{a}{W}\right)}{\sigma_yB}\sqrt{\frac{r_P}{6\pi W}}F}\right\} \\
& - \frac{F^2a^2(1-\nu^2)}{BEI}\frac{F^2f^2\left(\frac{a}{W}\right)}{6\pi\sigma_y^3B^2W}\left(1 + \frac{4}{3}\frac{F^2f^2\left(\frac{a}{W}\right)}{6\pi\sigma_y^2B^2Wa} + \frac{1}{2}\frac{F^4f^4\left(\frac{a}{W}\right)}{36\pi^2\sigma_y^4B^4W^2a^2}\right)\cdot\frac{\mathrm{d}\sigma_y}{\mathrm{d}a} \\
& - \frac{A'W}{B}\frac{\mathrm{d}}{\mathrm{d}\sigma_y}\int_0^F \frac{F^n}{r_P(W-a) - \frac{f^2\left(\frac{a}{W}\right)r_P}{6\pi B^2W\sigma_y^2}F^2}\mathrm{d}F\cdot\frac{\mathrm{d}\sigma_y}{\mathrm{d}a} + \frac{f^2\left(\frac{a}{W}\right)(1-\nu^2)F^3}{6\pi m\sigma_y^4EB^3W}\cdot\frac{1-r_P}{r_P}\frac{\mathrm{d}\sigma_y}{\mathrm{d}a} + \frac{2(1-\nu^2)W}{EBmr_P\sigma_y^3}F\frac{\mathrm{d}\sigma_y}{\mathrm{d}a} \\
& - \frac{(1-\nu^2)W^{\frac{5}{2}}(6\pi)^{\frac{3}{2}}B^2}{2mEf^3\left(\frac{a}{W}\right)r_P^2}\left\{2\sigma_y\cdot\ln\frac{\sqrt{r_P(W-a)} + \frac{f\left(\frac{a}{W}\right)}{\sigma_yB}\sqrt{\frac{r_P}{6\pi W}}F}{\sqrt{r_P(W-a)} - \frac{f\left(\frac{a}{W}\right)}{\sigma_yB}\sqrt{\frac{r_P}{6\pi W}}F}\cdot\frac{\frac{2f\left(\frac{a}{W}\right)}{B}r_P\sqrt{\frac{W-a}{6\pi W}}}{r_P(W-a) - \frac{f^2\left(\frac{a}{W}\right)}{\sigma_y^2B^2}\frac{r_P}{6\pi W}F^2}\right\}\frac{\mathrm{d}\sigma_y}{\mathrm{d}a} \\
& - \left\{\frac{A'}{B}\frac{r_P-1}{r_P}\left(F^n + \frac{F^{n+1}}{(n+1)^2}\right) + \frac{A'W}{B}\frac{\mathrm{d}}{\mathrm{d}n}\int_0^F \frac{F^n}{r_P(W-a) - \frac{f^2\left(\frac{a}{W}\right)r_P}{6\pi B^2W\sigma_y^2}F^2}\mathrm{d}F\right\}\cdot\frac{\mathrm{d}n}{\mathrm{d}a}
\end{aligned} \qquad \text{(Eq 6)}$$

where F is the corresponding force to each J value in force-displacement curve, A is the crack length at corresponding J, W is the specimen width, $F(a/W)$ is the shape factor, r_P is the rotational factor which is equal to 0.44, m is a constant and is equal to 1 and 2 for plane-stress and plane-strain conditions, respectively, A' is the power-law relation constant of load-displacement curve of FGS, and n is the work-hardening exponent in load-displacement curve.

J-R curve of the composites in crack arrester configuration was determined and J_{IC} values were obtained by these curves was calculated. The obtained results are listed in Table 3, which shows relatively good agreement, by experimental data.

For further studies progress are in try to simulate fracture toughness of FGSs by finite element method in both crack divider and crack arrester configurations.

4. Conclusions

From the above discussions, it may be concluded the arrangement of primary electrodes' pieces and the volume fraction of containing phases are the key factors determine the fracture toughness of the composites in crack divider configuration. On the other hand, the position of the crack tip, the distance of the crack tip with respect to the intermediate bainite and martensite layers, and experiencing upward or downward fracture toughness gradient are the most important factors which affect the final fracture toughness of the composites in crack arrester configuration.

It has been concluded that J_{IC} test could predict the absorbed energy of the specimens more accurate than Charpy impact test in both crack divider and crack arrester configurations where, martensite layer could not play the major role in determining the absorbed energy.

In both crack divider and crack arrester configurations, for αβγ and γMγ composites, only the fracture toughness of AISI 1020 steel has been improved and no improvement in fracture toughness of AISI 316 steel has been observed.

References

1. H.A. Bahr, H. Balke, T. Fett, I. Hofinger, G. Kirchhoff, D. Munz, A. Neubrand, A.S. Semenov, H.J. Weiss, and Y.Y. Yang, Cracks in Functionally Graded Materials, *Mater. Sci. Eng. A*, 2003, **362**, p 2–16
2. Z.H. Jin, G.H. Paulino, and R.H. Dodds, Jr., Cohesive Fracture Modeling of Elastic-Plastic Crack Growth in Functionally Graded Materials, *Eng. Fract. Mech.*, 2003, **70**, p 1885–1912
3. K. Tohgo, T. Suzuki, and H. Araki, Evaluation of R-Curve Behavior of Ceramic-Metal Functionally Graded Materials by Stable Crack Growth, *Eng. Fract. Mech.*, 2005, **72**, p 2359–2372
4. C.E. Rousseau and H.V. Tippur, Compositionally Graded Materials with Cracks Normal to the Elastic Gradient, *Acta Mater.*, 2000, **48**(16), p 4021–4033
5. O. Kolednik, The Yield Stress Gradient Effect in Inhomogeneous Materials, *Int. J. Sol. Struct.*, 2000, **37**, p 781–808
6. T.L. Becker, Jr., R.M. Cannon, and R.O. Ritchie, Statistical Fracture Modeling: Crack Path and Fracture Criteria with Application to Homogeneous and Functionally Graded Materials, *Eng. Fract. Mech.*, 2002, **69**, p 1521–1555
7. B. Bezensek and J.W. Hancock, The Toughness of Laser Welded Joints in the Ductile-Brittle Transition, *Eng. Fract. Mech.*, 2007, **74**, p 2395–2419
8. J.-M. Aghazadeh and M.H. Shahosseinie, Transformation Characteristics of Functionally Graded Steels Produced by Electroslag Remelting, *Met. Mater. Trans. A*, 2005, **36**, p 3471–3476
9. A. Nazari, J.-M. Aghazadeh, Modeling Impact Energy of Functionally Graded Steels in Crack Divider Configuration, *Mater. Sci. Technol.*, 2010, **26**(11), p 1377–1383
10. A. Nazari and J.-M. Aghazadeh, Impact Energy of Functionally Graded Steels with Crack Divider Configuration, *J. Mater. Sci. Technol.*, 2009, **25**(6), p 847–852
11. A. Nazari, J.-M. Aghazadeh, Impact Energy of Functionally Graded Steels in Crack Arrester Configuration, *J. Mater. Eng. Perform.*, 2010, **19**, p 1058–1064
12. J.-M. Aghazadeh, M.H. Shahosseinie, and R.-N. Parastar, Tensile Behavior of Functionally Graded Steels Produced by Electroslag Remelting, *Met. Mater. Trans. A*, 2006, **37**, p 2125–2132
13. ASTM E1820, Standard Test Method for Measurement of Fracture Toughness, Annual book of ASTM Standards, ASTM, Philadelphia, PA; 2001
14. J.W. Hutchinson, Singular Behavior at the End of a Tensile Crack in a Hardening Material, *J. Mech. Phys. Sol*, 1968, **16**, p 13–31
15. J.R. Rice and G.F. Rosengeren, Plane Strain Deformation Near a Crack Tip in a Power-Law Hardening Material, *J. Mech. Phys. Sol*, 1968, **16**, p 1–12
16. F. Carreno, J. Chao, M. Pozuelo, and O.A. Ruano, Microstructure and Fracture Properties of an Ultrahigh Carbon Steel-Mild Steel Laminated Composite, *Scripta Mater.*, 2003, **48**, p 1135–1140
17. Z.H. Jin and R.H. Dodds, Jr., Crack Growth Resistance Behavior of a Functionally Graded Material: Computational Studies, *Eng. Fract. Mech.*, 2004, **71**, p 1651–1672